aerospace

MDPI

Article

A Study on Intercepting Highly Maneuvering Targets Using an Input Estimation Approach and Improved Particle Swarm Guidance Law

Yung-Lung Lee [1,*] and Wan-Yu Yu [2]

[1] Department of Power Vehicle and Systems Engineering, Chung Cheng Institute of Technology, National Defense University, No. 75, Shiyuan Rd., Daxi Dist., Taoyuan 335, Taiwan
[2] Department of Computer Science and Information Engineering, Chung Cheng Institute of Technology, National Defense University, No. 75, Shiyuan Rd., Dashi Jen, Taoyuan 335, Taiwan; csvillea@gmail.com
* Correspondence: yunglunglee84@ccit.ndu.edu.tw

Abstract

Ballistic missiles exhibit high velocities and rapid maneuverability after atmospheric reentry, posing substantial challenges for anti-ballistic missile (ABM) interception. This paper presents an integrated interception framework that combines an input estimation method with an improved particle swarm optimization-based guidance law (IPSOG). The input estimation approach processes noisy radar measurements to estimate target states in the presence of unknown system inputs and measurement noise. Its performance is evaluated through simulations and compared with the extended Kalman filter (EKF), demonstrating improved estimation accuracy and robustness under highly maneuvering conditions. An improved particle swarm optimization algorithm is employed to design the interceptor guidance law. Compared with conventional proportional navigation guidance (PNG), the proposed guidance method provides enhanced adaptability to target maneuvers. Numerical simulations are conducted to evaluate interception performance against maneuvering ballistic missile targets. Results show reductions in miss distance and interception time while maintaining lower average lateral acceleration and a larger effective interception region. These results indicate that the proposed framework improves both target state estimation and interceptor guidance performance for highly maneuvering ballistic missile targets.

Keywords: anti-ballistic missile (ABM); extended Kalman filter (EKF); input estimation (IE); proportional navigation guidance (PNG); improved particle swarm optimization guidance (IPSOG)

Check for updates

Received: 28 January 2026
Revised: 15 March 2026
Accepted: 31 March 2026
Published: 2 April 2026

Copyright: © 2026 by the authors. Licensee MDPI, Basel, Switzerland. This article is an open access article distributed under the terms and conditions of the Creative Commons Attribution (CC BY) license.

1. Introduction

Ballistic missiles (BMs) have evolved from early unguided weapons into highly capable delivery systems and now represent a major challenge for modern missile defense architectures. Owing to their long range, high terminal velocity, small radar cross section, and limited engagement time, ballistic missiles are inherently difficult to intercept. Although early ballistic missile systems were constrained by poor terminal accuracy, advances in reentry vehicle (RV) guidance and control have significantly improved terminal precision. A notable example is the Pershing II RV, which employed aerodynamic control surfaces in combination with a radar area correlation (RAC) terminal guidance scheme to enable

trajectory correction during reentry and reduce impact error [1]. Building on these developments, modern ballistic missile systems increasingly incorporate deliberate maneuvering during the reentry phase to enhance both terminal accuracy and survivability. Reentry maneuvering introduces substantial deviations from classical ballistic trajectories and produces highly nonlinear target motion, which significantly complicates radar-based target tracking and interceptor guidance. Missile defense systems originally designed under non-maneuvering or weakly maneuvering assumptions often experience degraded tracking and interception performance when confronted with such targets. In addition, maneuvering reentry vehicles have enabled the development of advanced offensive systems, including anti-ship ballistic missiles intended to penetrate layered naval air- and missile-defense networks and engage high-value maritime assets [2]. The emergence of these systems has intensified the demand for missile defense technologies capable of accurately tracking and intercepting highly maneuvering ballistic targets. Consequently, two technical challenges arise: reliable radar-based estimation of maneuvering target states in the presence of measurement noise and modeling uncertainty, and the design of interceptor guidance laws that can effectively accommodate rapid and unpredictable target maneuvers. These issues have attracted sustained research interest in the missile defense and guidance communities [3–6]. The present study addresses these challenges by investigating robust target state estimation and adaptive guidance law design for the interception of maneuvering ballistic missiles.

Target tracking can be accomplished using either active or passive sensing systems. For ballistic target trajectory estimation, several studies have proposed angle-only measurement approaches based on passive sensors [7–9]. In these methods, the reentry trajectory of a ballistic target is estimated using two-dimensional measurements, namely azimuth and elevation, obtained from a moving passive sensor platform. Although angle-only measurements provide limited observability, the proposed estimators have demonstrated satisfactory performance under certain sensor configurations and operational conditions. Numerical simulation results indicate that the approach can accurately estimate the trajectory of a non-maneuvering target during the reentry phase. Furthermore, the estimated trajectory can be incorporated into missile guidance laws to support target interception. In active sensor target tracking, radar sensors provide measurements of target states such as relative position and velocity. However, these measurements are inevitably contaminated by noise arising from sensor limitations, environmental effects, and signal processing errors. Consequently, suppressing measurement noise and accurately estimating the true target state remain fundamental challenges in radar-based tracking systems. The performance of a target state estimator strongly depends on the selection of an appropriate target motion model and a filtering algorithm capable of mitigating the effects of process uncertainty and measurement noise. Target motion models are generally categorized as non-maneuvering or maneuvering. The non-maneuvering class typically assumes constant-velocity motion along a straight-line trajectory, while other motion patterns are considered maneuvering. The constant-velocity (CV) model is widely used for non-maneuvering targets due to its simplicity and computational efficiency. In contrast, the constant-acceleration (CA) model represents the simplest maneuvering target model and is commonly used to describe targets undergoing mild or slowly varying maneuvers [10,11]. Although these models are effective under their respective assumptions, their applicability is often limited when the target performs abrupt or high-magnitude maneuvers, as is typical for maneuvering reentry vehicles. Filtering algorithms for target tracking can be broadly divided into two categories. The first consists of minimum-error filters, which are typically based on heuristic or steady-state formulations, with the α–β filter serving as a representative example [12,13]. The second category includes minimum error covariance filters, among which the Kalman filter (KF) is the most prominent. Introduced by Kalman in 1960, the KF provides an optimal

recursive estimation framework for linear dynamical systems with Gaussian noise [14]. Because many practical tracking problems involve nonlinear system dynamics and measurement relationships, the assumptions of the standard KF are often violated. To address this limitation, the extended Kalman filter (EKF) was developed by linearizing the nonlinear system and measurement models about the current state estimate. The EKF has therefore been widely applied in numerous guidance and control applications, including communications systems, control engineering, satellite navigation, image processing, and radar target tracking [15]. Nevertheless, the linearization inherent in the EKF can degrade estimation accuracy and robustness when the target exhibits strong nonlinear motion or high maneuverability. This limitation motivates the development of alternative estimation approaches for maneuvering ballistic targets.

With respect to the application of KF to ballistic trajectory estimation, Shi et al. [16] employed a Kalman filtering approach combined with a point-mass ballistic motion model to develop a ballistic trajectory estimation framework. Radar-measured flight trajectories were processed through the proposed filter, yielding state estimates that closely approximated the true ballistic trajectories. Because missile dynamics are inherently nonlinear, the standard linear KF cannot be directly applied to ballistic missile tracking problems. To address this limitation, Farina et al. [17] investigated reentry-phase target tracking using four nonlinear filtering techniques: the EKF, the covariance analysis describing function technique (CADFT), the unscented Kalman filter (UKF), and the particle filter (PF). A comprehensive comparative evaluation of estimation performance was conducted. Simulation results showed that the estimation error standard deviations of all four filters approached the Cramér–Rao lower bound (CRLB). Owing to its significantly lower computational complexity relative to the other methods, the EKF was shown to provide the best overall trade-off between estimation accuracy and computational efficiency. Although the EKF and its variants have been demonstrated to be effective and high-performance estimation algorithms, a major limitation arises when the system inputs are unknown. In such cases, state estimation must be performed without explicit input modeling, which can result in degraded estimation accuracy. Consequently, the incorporation of input estimation techniques into the filtering framework has been shown to mitigate the effects of model uncertainty and to significantly improve estimation performance [18].

Input estimation (IE) was first introduced by Chan et al. in 1979 [19] to address the problem of tracking targets undergoing abrupt dynamic changes. Subsequently, Bogler [20] extended this concept to maneuvering target tracking by employing a batch-form generalized least squares method (GLSM) to estimate unknown acceleration inputs. In this framework, input estimation was used to detect target maneuvers and to correct the filter state. However, owing to its batch-processing structure, this method is limited to post-processing applications and is therefore unsuitable for real-time estimation [21]. To meet real-time estimation requirements, Tuan et al. proposed a recursive input estimation scheme in 1996 [22]. This approach constructs regression equations based on a KF formulation without input terms and exploits the innovation residual sequence generated during the filtering process. The unknown input is recursively estimated using a recursive least squares method (RLSM) and subsequently incorporated into a KF with input terms to obtain improved state estimates. This recursive framework not only enhances estimation accuracy but also significantly reduces computational complexity. Lee et al. further extended the input estimation framework to nonlinear system models by integrating an input estimator with an EKF (EKF + IE), thereby developing an adaptive Kalman filter (AKF). This AKF-based approach was applied to real-time trajectory estimation of tactical ballistic missiles and demonstrated improved estimation performance [23]. In addition, Chen et al. replaced the fixed weighting factor in the recursive least squares estimator (RLSE) with

a fuzzy weighting function and proposed the fuzzy weighting input estimation method (FWIEM) [24]. By incorporating a fuzzy logic system into the least squares estimator, the proposed method achieved rapid tracking of input signals while maintaining effective noise suppression, resulting in substantial performance improvements. Motivated by these developments, the present study adopts an EKF incorporating input estimation techniques to evaluate state estimation performance for high-speed maneuvering targets.

The selection of an appropriate guidance strategy is a critical issue in missile guidance law design, as it directly affects interception accuracy and overall engagement performance in precision-guided missile systems. Various guidance laws have been developed for missile interception, including pure pursuit, parallel navigation, three-point guidance, and proportional navigation (PN) [25]. Among these approaches, proportional navigation guidance (PNG) remains the most widely adopted method for terminal-phase missile guidance due to its simplicity, robustness, and favorable stability characteristics [26]. In PNG, the missile lateral acceleration command is proportional to the rate of change in the line-of-sight (LOS) angle between the interceptor and the target, enabling the interceptor to generate a lead-angle trajectory that facilitates interception. In atmospheric interception scenarios involving ballistic missile reentry, engagement durations are typically short, and relative velocities are extremely high. Consequently, the performance of the interceptor guidance law plays a decisive role in determining interception effectiveness. Several hybrid guidance strategies have been proposed to enhance performance. For instance, Lee et al. [27] introduced a hybrid PN and command-to-line-of-sight (CLOS) scheme that allows the interceptor to converge toward a collision trajectory during the early engagement stage, thereby reducing corrective maneuvers in the terminal phase. Despite these developments, the emergence of hypersonic glide vehicles and highly maneuverable reentry targets poses significant challenges to conventional guidance laws [28]. A key limitation of PNG lies in its implicit assumption that the interceptor velocity exceeds that of the target. This assumption is often violated in atmospheric interception scenarios, which can significantly degrade interception performance. Furthermore, strict terminal guidance initiation conditions and large lateral acceleration demand during the mid-to-late terminal phase may increase miss distance. These challenges highlight the need for improved state estimation and guidance strategies capable of handling unknown target maneuvers. Motivated by these limitations, this study investigates the integration of input estimation and adaptive filtering techniques to improve guidance performance. Specifically, an extended Kalman filter (EKF) with input estimation is developed to mitigate the effects of unknown maneuver-induced inputs during the target reentry phase and enhance interceptor guidance against highly maneuvering ballistic targets [29–32].

Particle swarm optimization (PSO) is a heuristic global optimization algorithm originally proposed by Kennedy and Eberhart in 1995 [33,34]. Owing to its simple computational structure, ease of implementation, and rapid convergence characteristics, PSO has been widely applied to a broad class of optimization problems. The algorithm employs a population-based search strategy governed by a set of simple update rules that emulate the social foraging behavior observed in biological swarms, enabling efficient exploration and exploitation of the solution space. PSO has been successfully utilized in numerous engineering applications, including optimal control system design, system parameter identification, reliability analysis, trajectory optimization, machine learning, and combinatorial optimization of discrete systems [35,36]. In Ref. [37], PSO was integrated into missile guidance law design, and its performance was evaluated against conventional pure pursuit guidance for intercepting maneuvering targets in both air-to-air and air-to-ground engagement scenarios. Simulation results demonstrated that PSO-based guidance laws (PSOG) were capable of significantly reducing interception time relative to conventional methods. Motivated by these

prior studies, PSO is adopted in the present work as the optimization framework for ABM guidance law design. By exploiting the rapid convergence and global search capabilities of PSO, optimized guidance commands are generated to enhance interception performance against BMs, particularly under high-speed and maneuvering engagement conditions.

The remainder of this paper is organized as follows. Section 1 introduces the research motivation and reviews related to the work. Section 2 presents the modeling of maneuvering ballistic missile trajectories. Section 3 describes the proportional navigation guidance law and the proposed IPSOG-based guidance scheme. Section 4 introduces the EKF, input estimation algorithms, and the integrated interception framework. Section 5 presents simulation results and performance analysis. Section 6 concludes the paper and discusses future work.

2. Maneuvering Target Modeling

In general, the flight of a BM can be divided into three distinct phases, as illustrated in Figure 1. The first is the boost phase, which corresponds to the launch and powered acceleration of the missile. This phase typically lasts approximately 100–200 s. The second is the midcourse phase, during which the warhead separates from the booster and travels primarily under inertial motion in a near-vacuum environment. This phase generally has the longest duration; for intercontinental ballistic missiles, it may extend for several thousand seconds. The third is the reentry phase, which begins when the BM reenters the atmosphere and continues until impact. To improve terminal accuracy, BMs may perform trajectory corrections during this phase. Consequently, the flight path deviates from a purely ballistic free-fall trajectory and exhibits maneuvering characteristics, as shown in Figure 1. Because the primary focus of this study is the interception of BMs during the terminal engagement, only the target motion in the reentry phase is considered and modeled in the subsequent analysis.

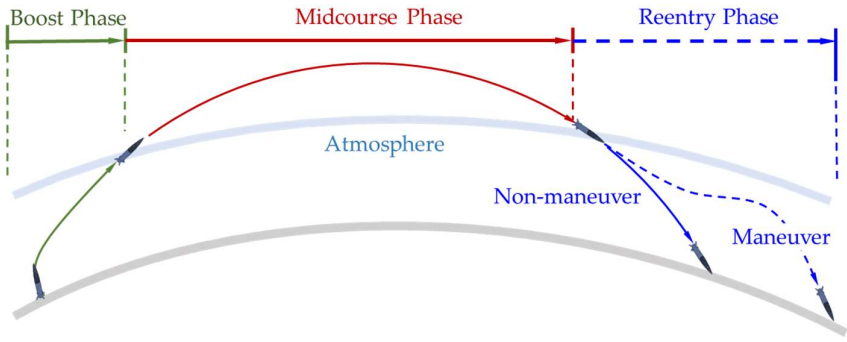
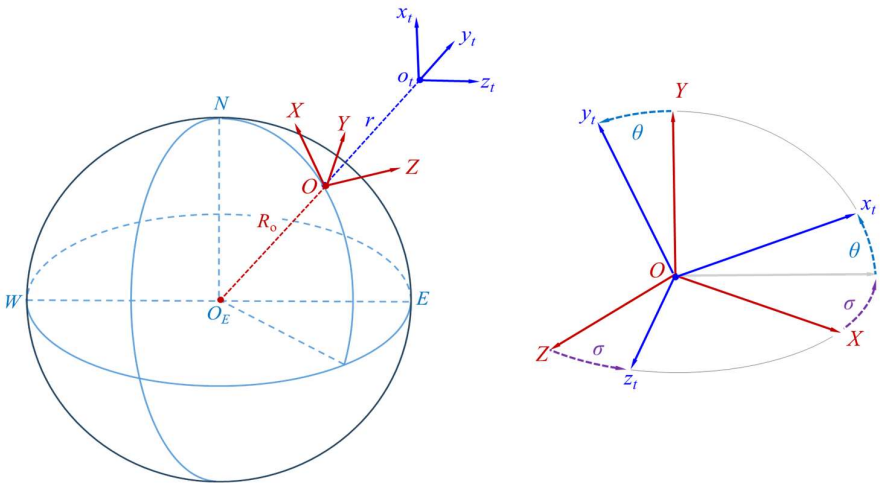


Figure 1. Schematic of the BM flight path.

The motion of a BM can be decomposed into translational motion of the center of mass and rotational motion about the center of mass. Since the rotational motion about the center of mass has a negligible influence compared with the translational motion, this study considers only the translational motion of the BM's center of mass. The inertial coordinate system O–XYZ and the body-fixed coordinate system o_t–$x_t y_t z_t$ employed in this study are illustrated in Figure 2a. The transformation between the two coordinate systems is obtained by first rotating an angle σ about the Y-axis, followed by a rotation of an angle θ about the new Z-axis, i.e., following the yaw (σ)–pitch (θ) rotation sequence, as shown in Figure 2b. The coordinate transformation between the two systems is expressed as follows.

$$\begin{bmatrix} x_t \\ y_t \\ z_t \end{bmatrix} = \begin{bmatrix} \cos\sigma\cos\theta & \sin\theta & -\sin\sigma\cos\theta \\ -\cos\sigma\sin\theta & \cos\theta & \sin\sigma\sin\theta \\ \sin\sigma & 0 & \cos\sigma \end{bmatrix} \begin{bmatrix} x \\ y \\ z \end{bmatrix} = \mathbf{H_O} \begin{bmatrix} x \\ y \\ z \end{bmatrix} \tag{1}$$



(**a**) (**b**)

Figure 2. (**a**) Inertial and body-fixed coordinate systems; (**b**) relationship between the inertial and body-fixed coordinate systems.

Considering that the flight duration of the BM after atmospheric reentry is relatively short, the effect of Earth's rotation on the flight trajectory is neglected. In addition, the BM is modeled as a point mass, and the influence of control forces generated by the attitude control system is ignored. Furthermore, the BM is assumed to be unpowered during atmospheric reentry. Under these assumptions, the equations of motion can be simplified as follows [10]:

$$\begin{cases} \dot{v} = (R_{xh}/m) + g_{xh} \\ \dot{\theta} = \left(R_{yh}/mv\right) + g_{yh}/v \\ \dot{\sigma} = -(R_{zh}/mv\cos\theta) - g_{zh}/(v\cos\theta) \\ \dot{x} = v\cos\theta\cos\sigma \\ \dot{y} = v\sin\theta \\ \dot{z} = -v\cos\theta\sin\sigma \end{cases} \tag{2}$$

where m and v denote the mass and velocity of the ballistic missile, respectively. g_{xh}, g_{yh} and g_{zh} denote the components of the gravitational acceleration projected onto the body-fixed coordinate system. The corresponding relationships are given as follows:

$$\begin{bmatrix} g_{xh} \\ g_{yh} \\ g_{zh} \end{bmatrix} = \begin{bmatrix} \cos\sigma\cos\theta & \sin\theta & -\sin\sigma\cos\theta \\ -\cos\sigma\sin\theta & \cos\theta & \sin\sigma\sin\theta \\ \sin\sigma & 0 & \cos\sigma \end{bmatrix} \begin{bmatrix} x \\ y + R_0 \\ z \end{bmatrix} \left(-\frac{g}{r}\right) \tag{3}$$

$$r = \sqrt{x^2 + (y + R_0)^2 + z^2} \tag{4}$$

where R_0 represents the radius of the Earth. R_{xh}, R_{yh}, and R_{zh} are the projections of air resistance in the BM body coordinate system, and their relationships are as follows:

$$\begin{bmatrix} R_{xh} \\ R_{yh} \\ R_{zh} \end{bmatrix} = \begin{bmatrix} -C_x \\ C_y \\ C_z \end{bmatrix} qS \tag{5}$$

$$q = \rho v^2/2 \tag{6}$$

where ρ is the atmospheric density and S is the reference area of the BM. Because the BM's flight altitude (h) varies significantly, the atmospheric density ρ changes with altitude, and is expressed as [38].

$$\begin{cases} \rho = 0.002378e^{-h/30{,}000} & h < 30{,}000 \text{ m} \\ \rho = 0.0034e^{-h/22{,}000} & h \geq 30{,}000 \text{ m} \end{cases} \tag{7}$$

C_x, C_y, and C_z are the drag coefficients, and their relationships with the angle of attack α and the sideslip angle β are given as follows:

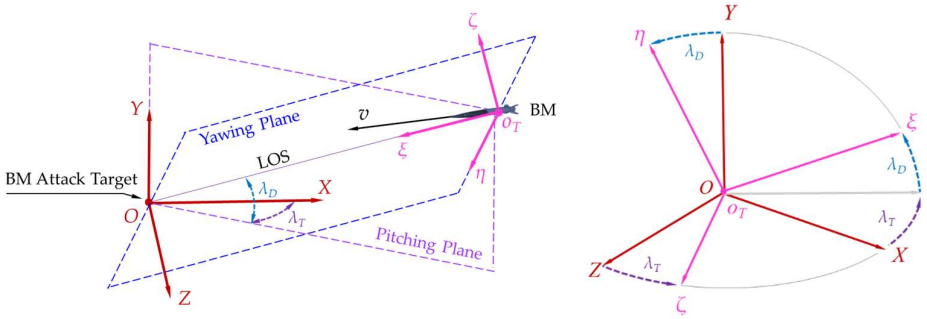
$$\begin{cases} C_x = C_{x0} + C_x^{\alpha}\left(\alpha^2 + \beta^2\right) \\ C_y = C_y^{\alpha}\alpha \\ C_z = C_z^{\alpha}\beta \end{cases} \tag{8}$$

where C_{x0}, C_x^{α}, C_y^{α} and C_z^{α} are parameters of the drag formula.

Based on the equations of motion of the BM given in Equation (2), the state vector is defined as $\mathbf{X} = [v, \theta, \sigma, x, y, z]^T$, where v denotes the BM velocity, θ and σ represent the velocity-direction angles, and x, y, and z denote the Cartesian coordinates of the center-of-mass position. The control variables are chosen as the angle of attack α and the sideslip angle β. Accordingly, the BM flight trajectory is uniquely determined by specifying the control histories of α and β.

For the formulation of the BM guidance law, terminal constraints are imposed on both the impact position and the terminal flight-path angle of the BM. The engagement kinematics, defined with respect to the relative motion between the ground target and the BM, are decomposed into the pitch and yaw planes, as illustrated in Figure 3a. In this representation, λ_D and λ_T denote the LOS angles associated with the downrange and cross-range directions, respectively. The coordinate transformation between the ground target-fixed frame O-XYZ and the LOS frame o_T-$\xi\eta\zeta$ is illustrated in Figure 3b, and the corresponding transformation matrix used in the guidance and trajectory optimization formulation is given in Equation (9).

$$\begin{bmatrix} \xi \\ \eta \\ \zeta \end{bmatrix} = \mathbf{S_o} \begin{bmatrix} x \\ y \\ z \end{bmatrix} = \begin{bmatrix} \cos\lambda_D \cos\lambda_T & \sin\lambda_D & -\cos\lambda_D \sin\lambda_T \\ -\sin\lambda_D \cos\lambda_T & \cos\lambda_D & \sin\lambda_D \sin\lambda_T \\ \sin\lambda_T & 0 & \cos\lambda_T \end{bmatrix} \begin{bmatrix} x \\ y \\ z \end{bmatrix} \tag{9}$$



(**a**) (**b**)

Figure 3. (**a**) Schematic representation of the pitch and yaw planes of the BM relative to the target; (**b**) coordinate transformation between the target-fixed frame and the LOS coordinate frame.

The projections of the BM velocity v, pitch angle θ, and yaw angle σ onto the LOS coordinate frame are expressed in Equations (10) and (11) and are used to formulate the relative kinematics and terminal constraints in the guidance and trajectory optimization problem.

$$\begin{bmatrix} v_\xi \\ v_\eta \\ v_\zeta \end{bmatrix} = \mathbf{S_O} \begin{bmatrix} v_x \\ v_y \\ v_z \end{bmatrix} = \mathbf{S_O} \begin{bmatrix} \dot{x} \\ \dot{y} \\ \dot{z} \end{bmatrix} \tag{10}$$

$$\begin{bmatrix} \dot{\gamma}_\xi \\ \dot{\gamma}_T \\ \dot{\gamma}_D \end{bmatrix} = \mathbf{S_O} \begin{bmatrix} -\dot{\theta}\sin\sigma \\ \dot{\sigma} \\ -\dot{\theta}\cos\sigma \end{bmatrix} \tag{11}$$

Here, $\dot{\gamma}_D$ and $\dot{\gamma}_T$ denote the angular rates in the pitch and yaw planes, respectively. The relationship between the LOS angle rates and the BM velocity components expressed in the LOS coordinate frame is given in Equation (12), which governs the relative kinematic evolution used in the guidance formulation. The expression for the time-to-go T_g representing the remaining flight time required for the warhead to reach the target location, is provided in Equation (13) and is employed as a key parameter in the trajectory optimization process.

$$\begin{cases} \dot{\lambda}_D = v_\eta / R \\ \dot{\lambda}_T = -v_\zeta / (R\cos\lambda_D) \end{cases} \tag{12}$$

$$T_g = R / v_\xi \tag{13}$$

To regulate the terminal flight-path angle, the optimal guidance law developed by Chen et al. [39] is employed as a reference, as shown in Equation (14).

$$\begin{cases} \dot{\gamma}_D = -4\dot{\lambda}_D - 2(\lambda_D + \gamma_{DF})/T_g \\ \dot{\gamma}_T = 3\dot{\lambda}_T\cos\lambda_D \end{cases} \tag{14}$$

Here, γ_{DF} represents the terminal flight-path angle. As shown in Figure 3a, the LOS angles λ_D and λ_T are computed as follows.

$$\begin{cases} \lambda_D = \tan^{-1}\left(y/\sqrt{x^2+z^2}\right) \\ \lambda_T = \tan^{-1}(-z/x) \end{cases} \tag{15}$$

The kinematic relationships between the pitch angle θ, the yaw angle σ, and the corresponding LOS angles are described as follows.

$$\begin{cases} \dot{\theta} = \frac{-\dot{\gamma}_D}{\cos(\lambda_T - \sigma)} \\ \dot{\sigma} = \frac{1}{\cos\lambda_D}\left[\dot{\gamma}_T - \dot{\gamma}_D\tan(\lambda_T - \sigma)\sin\lambda_D\right] \end{cases} \tag{16}$$

By equating $\dot{\theta}$ and $\dot{\sigma}$ in Equations (2) and (16), the BM trajectory control variables α and β are obtained as follows.

$$\alpha = \frac{mv\left[4T_g\dot{\lambda}_D + 2(\lambda_D + \gamma_{DF})\right]}{C_y^\alpha qST_g\cos(\lambda_T - \sigma)} - \frac{mg_{yh}}{C_y^\alpha qS} \tag{17}$$

$$\beta = \frac{-mv\cos\theta}{C_y^\alpha qS\cos\lambda_D}\left\{3\dot{\lambda}_T\cos\lambda_D + \left[4\dot{\lambda}_D + \frac{2(\lambda_D + \gamma_{DF})}{T_g}\right]\tan(\lambda_T - \sigma)\sin\lambda_D\right\} - \frac{mg_{zh}}{C_y^\alpha qS} \tag{18}$$

3. Anti-Ballistic Missile Guidance Law

3.1. Proportional Navigation Guidance

PNG is derived from the principle that the missile lateral acceleration is proportional to the rate of change in the LOS angle between the interceptor (ABM) and the target (BM). In a three-dimensional coordinate framework, effective target interception can be achieved by appropriately commanding the ABM lateral accelerations—namely, the yaw acceleration a_y and the pitch acceleration a_p—to drive the LOS rate to zero.

Let $M(x_M, y_M, z_M)$ and $T(x_T, y_T, z_T)$ denote the position vectors of the ABM and the BM, respectively. The relative geometry between the interceptor (ABM) and the target (BM) in three-dimensional space is depicted in Figure 4, where σ_M and θ_M denote the missile yaw and pitch angles, respectively. The quantity r_{TM} represents the relative distance between the missile and the target projected onto the X-Y plane. The relative distance R_{TM} between the ABM and the BM is given by Equation (19):

$$R_{TM} = \sqrt{x_{TM}^2 + y_{TM}^2 + z_{TM}^2} \tag{19}$$

where

$$\begin{cases} x_{TM} = x_T - x_M \\ y_{TM} = y_T - y_M \\ z_{TM} = z_T - z_M \end{cases} \tag{20}$$

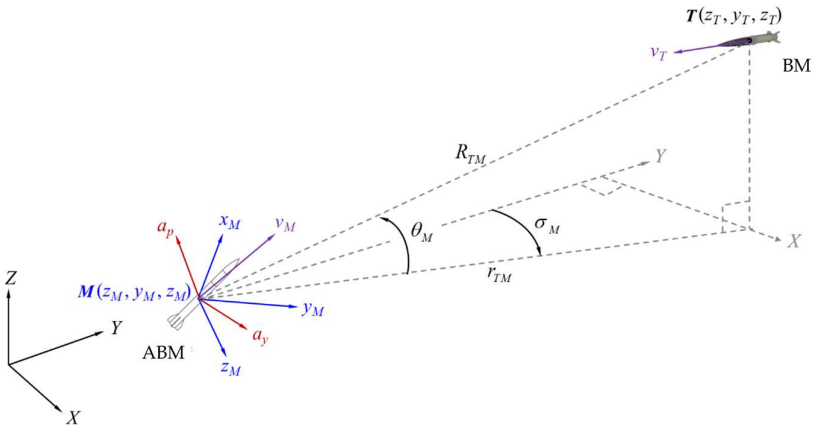


Figure 4. Three-dimensional engagement geometry between the ABM and the BM.

The transformation matrix from the inertial frame to the body frame, denoted as $\mathbf{B_I}$, is given by:

$$\mathbf{B_I} = \begin{bmatrix} \cos\theta_M \cos\sigma_M & \cos\theta_M \sin\sigma_M & -\sin\theta_M \\ -\sin\sigma_M & \cos\sigma_M & 0 \\ \sin\theta_M \cos\sigma_M & \sin\theta_M \sin\sigma_M & \cos\theta_M \end{bmatrix} \tag{21}$$

where $\sin\theta_M$, $\cos\theta_M$, $\sin\sigma_M$ and $\cos\sigma_M$ may be expressed as:

$$\sin\theta_M = -z_{TM}/R_{TM} \tag{22}$$

$$\cos\theta_M = r_{TM}/R_{TM} \tag{23}$$

$$\sin\sigma_M = y_{TM}/r_{TM} \tag{24}$$

$$\cos\sigma_M = x_{TM}/r_{TM} \tag{25}$$

In the inertial reference frame, the ABM velocity $\boldsymbol{v_M}$ (v_{xM}, v_{yM}, v_{zM}), the BM velocity $\boldsymbol{v_T}$ (v_{xT}, v_{yT}, v_{zT}), and their relative velocity $v_{TM}\left(v'_{xTM}, v'_{yTM,}, v'_{zTM}\right)$ are defined, and the projection onto the missile body frame is expressed by Equation (26):

$$\begin{bmatrix} v'_{xTM} \\ v'_{yTM} \\ v'_{zTM} \end{bmatrix} = \mathbf{B}_{\mathrm{I}} \begin{bmatrix} v_{xTM} \\ v_{yTM} \\ v_{zTM} \end{bmatrix} \tag{26}$$

where v'_{xTM} denotes the closing velocity between the ABM and the BM. Accordingly, the lateral and longitudinal guidance acceleration commands, a_y and a_p are given by Equations (27) and (28), respectively:

$$a_y = N\dot{\sigma}_M v'_{xTM} \tag{27}$$

$$a_p = N\dot{\theta}_M v'_{xTM} \tag{28}$$

where N is the proportional navigation gain. $\dot{\theta}_M$ and $\dot{\sigma}_M$ denote the rates of change in the pitch angle and yaw angle, respectively. The missile regulates its yaw and pitch motions through the lateral and longitudinal acceleration commands a_y and a_p respectively, to achieve target interception.

3.2. Improved Particle Swarm Optimization–Based Guidance

PSO is a swarm intelligence–based optimization algorithm capable of solving nonlinear and multi-objective optimization problems. Due to its low computational complexity, limited number of tuning parameters, and rapid convergence characteristics, PSO is well suited for real-time missile guidance applications, particularly for the optimization of lateral acceleration commands. In conventional particle swarm optimization guidance (PSOG), interception is achieved by maintaining the LOS angle at zero. However, the performance of this approach deteriorates in the presence of target maneuvers, as the LOS angle constraint alone is insufficient to ensure robust interception. To overcome this limitation, an improved particle swarm optimization guidance (IPSOG) strategy is adopted [40]. In IPSOG, the LOS rate is selected as the fitness function, and the optimal lateral acceleration command is determined by minimizing this rate, thereby shaping an interception trajectory with enhanced robustness against target maneuvers. Chen et al. compared IPSOG with conventional PSOG and showed that IPSOG achieves better performance in terms of interception time and miss distance [40].

Since both IPSOG and PNG seek to drive the LOS rate to zero through lateral acceleration control, IPSOG may be interpreted as an optimized form of PNG, in which the guidance command is obtained through an online optimization process rather than a fixed proportional gain. In this study, a skid-to-turn (STT)-controlled missile is considered. The missile control actions are decomposed into pitch and yaw channels. During three-dimensional flight, variations in the longitudinal acceleration a_p and lateral acceleration a_y induce corresponding changes in the pitch and yaw angles, respectively, thereby modifying the missile trajectory. Based on this control framework, the computational procedure of the IPSOG algorithm is summarized as follows.

Step 1: Particle Swarm Initialization

A swarm consisting of n particles is initialized within the prescribed search space. The position of the jth particle at iteration i, denoted by $G_{i,j}$, represents a candidate guidance command vector composed of the commanded lateral accelerations in the pitch and

yaw channels. These control variables are defined in accordance with Equation (29) and constitute the decision variables in the trajectory optimization process.

$$\mathbf{G}_{i,j} = \begin{bmatrix} a_{pcom} \\ a_{ycom} \end{bmatrix} \tag{29}$$

Step 2: Formulation of Point-Mass Kinematic Model

The ABM is modeled as a point mass, and its three-dimensional equations of motion are derived under the point-mass assumption [41]. This modeling approach captures the essential translational dynamics required for guidance and trajectory optimization while neglecting rotational dynamics and higher-order effects. The resulting kinematic equations, which govern the evolution of the missile state under the applied acceleration commands, are given in Equations (30)–(36).

$$\dot{x}_M = v_M \cos\theta_M \cos\sigma_M \tag{30}$$

$$\dot{y}_M = v_M \cos\theta_M \sin\sigma_M \tag{31}$$

$$\dot{z}_M = v_M \sin\theta_M \tag{32}$$

$$\dot{\theta}_M = (a_p - g\cos\theta_M)/v_M \tag{33}$$

$$\dot{\sigma}_M = a_y/(v_M \cos\theta_M) \tag{34}$$

$$\dot{a}_p = (a_{pcom} - a_p)/\tau_m \tag{35}$$

$$\dot{a}_y = (a_{ycom} - a_y)/\tau_m \tag{36}$$

Here, τ_m denotes the actuator time constant. The variables a_{pcom} and a_{ycom} represent the commanded lateral accelerations along the y_M- and z_M-axes, respectively, whereas a_p and a_y denote the corresponding realized lateral accelerations along the same axes. The physical interpretation of all parameters is illustrated in Figure 4. By substituting the lateral acceleration commands generated in Step 1 into the equations of motion, the missile point-mass state is propagated forward in time for fitness evaluation within the guidance optimization loop.

Step 3: Fitness Function Formulation

The rates of change in the LOS elevation and azimuth angles between the ABM and the BM are employed to construct the fitness function $J_{i,j}$, as defined in Equations (37)–(39) [42]. This fitness function quantitatively measures the effectiveness of a candidate guidance command in reducing LOS motion, which is directly related to interception performance. Based on the resulting fitness values, particles exhibiting inferior performance are discarded, while those yielding superior performance are retained and propagated, thereby driving the swarm toward an optimal lateral acceleration command.

$$\dot{\sigma}_{i,j} = v'_{yTM}/R_{TM} \tag{37}$$

$$\dot{\theta}_{i,j} = v'_{zTM}/R_{TM} \tag{38}$$

$$J_{i,j} = \sqrt{\dot{\sigma}_{i,j}^2 + \dot{\theta}_{i,j}^2} \tag{39}$$

Step 4: Optimal Particle Selection Based on Fitness Evaluation

In this study, a parallel-approach guidance concept is adopted, in which the LOS between the ballistic missile and the interceptor is regulated to remain parallel over time,

corresponding to a zero LOS rate condition throughout the engagement. Under this framework, a smaller fitness value indicates a more effective lateral acceleration command for enforcing the desired LOS-rate behavior.

By comparing the fitness values of individual particles as well as those across the entire swarm, the individual-best and global-best particles are iteratively identified at each optimization cycle. Through this selection process, the optimal individual and global fitness values are obtained, as defined in Equations (40) and (41), thereby guiding the swarm toward the optimal acceleration command.

$$\begin{cases} Pbest_{i,j} = \mathbf{G}_{i,j}(\min(J_{i,j})) \\ PbestJ_{i,j} = \min(J_{i,j}) \end{cases} \quad if\ PbestJ_{i,j} > \min(J_{i,j}) \tag{40}$$

$$\begin{cases} Gbest_i = Pbest_{i,j}(\min(PbestJ_{i,j})) \\ GbestJ_i = \min(PbestJ_{i,j}) \end{cases} \quad if\ GbestJ_i > \min(PbestJ_{i,j}) \tag{41}$$

Step 5: Particle Velocity and Position Update

For each particle, the velocity $\mathbf{V}_{i+1,j}$ is updated according to Equation (42), incorporating the inertia, cognitive, and social components of the particle swarm optimization algorithm. Subsequently, the particle position $\mathbf{G}_{i+1,j}$ is updated using Equation (43), yielding a new candidate solution in the control space. The updated particle position corresponds to the commanded lateral accelerations (a_{pcom}, a_{ycom}), which are applied to the guidance law for state propagation and subsequent fitness evaluation.

$$\mathbf{V}_{i+1,j} = w \cdot \mathbf{V}_{i,j} + c_1 \cdot rand_{1_{i,j}}(Pbest_{i,j} - \mathbf{G}_{i,j}) + c_2 \cdot rand_{2_{i,j}}(Gbest_i - \mathbf{G}_{i,j}) \tag{42}$$

$$\mathbf{G}_{i+1,j} = \mathbf{G}_{i,j} + \mathbf{V}_{i+1,j} \tag{43}$$

In these equations, $i = 1, 2, \ldots, i_{\max}$, where $i_{\max}$ denotes the maximum number of iterations, and $j = 1, 2, \ldots, n$, where n is the total number of particles in the swarm. The variables $rand_1$ and $rand_2$ are independent random numbers uniformly distributed over the interval [0 1]. The parameter w represents the inertia weight. To improve convergence efficiency and solution stability in the guidance optimization process, the inertia weight is scheduled according to the formulation proposed in Ref. [37], as given in Equation (44).

$$w = w_{down} + \kappa(w_{up} - w_{down})/\kappa_{\max} \tag{44}$$

Here, w_{up} and w_{down} denote the upper and lower bounds of the inertia weight, respectively; κ represents the current generation index, and κ_{max} denotes the maximum number of generations.

In Equation (42), c_1 and c_2 denote the cognitive and social learning coefficients, respectively, which govern the balance between individual exploration and collective convergence. In this study, the linearly varying learning factors proposed by Ratnaweera et al. [42] are adopted, as given in Equations (45) and (46), to improve convergence characteristics and robustness of the optimization process in the guidance application.

$$c_1 = c_{1i} + \kappa(c_{1f} - c_{1i})/\kappa_{\max} \tag{45}$$

$$c_2 = c_{2i} + \kappa(c_{2f} - c_{2i})/\kappa_{\max} \tag{46}$$

In these expressions, c_{1i} and c_{2i} denote the initial values of the learning coefficients c_1 and c_2, respectively, while c_{1f} and c_{2f} represent their final values over the course of the optimization iterations. This parameter scheduling strategy facilitates a gradual transition

from global exploration to local exploitation, thereby enhancing convergence reliability in the guidance optimization process.

Step 6: Convergence Criterion Definition

At each iteration, the standard deviation of the particle positions $\mathbf{G}_{i,j}$ is evaluated according to Equation (47) to assess the convergence of the particle swarm:

$$\mathbf{S} = \left[\frac{1}{n-1} \sum_{j=1}^{n} (\mathbf{G}_j - \bar{\mathbf{G}})^2 \right]^{\frac{1}{2}} \tag{47}$$

where

$$\bar{\mathbf{G}} = \frac{1}{n} \sum_{j=1}^{n} \mathbf{G}_j \tag{48}$$

This metric provides a quantitative measure of solution dispersion in the control space and is used to determine whether the optimization process has sufficiently converged. If the standard deviation of $\mathbf{G}_{i,j}$ falls below a prescribed threshold, or if the iteration index i reaches the maximum allowable value i_{max}, the optimization is terminated and the corresponding global-best solution $Gbest_i$ is selected as the guidance command. Otherwise, the algorithm returns to Step 2 and continues the iterative procedure.

4. Ballistic Missile Trajectory Estimation Method

4.1. Extended Kalman Filter

A summary of the EKF prediction and update equations is presented in the following subsection. Consider a discrete-time nonlinear system with the following state and measurement models:

$$\mathbf{X}_{k+1} = f(\mathbf{X}_k) + \mathbf{w}_k \tag{49}$$

$$\mathbf{Z}_k = h(\mathbf{X}_k) + \mathbf{v}_k \tag{50}$$

In Equations (49) and (50), X_k denotes the system state vector, whereas $f(\cdot)$ and $h(\cdot)$ represent the nonlinear state transition and measurement functions, respectively. The terms $\mathbf{w}_k$ and $\mathbf{v}_k$ correspond to the process noise and measurement noise at time step k. Both noise processes are modeled as zero-mean, mutually uncorrelated Gaussian white sequences with known covariance properties. To facilitate recursive state estimation, the nonlinear system equations are linearized about the nominal (a priori) trajectory. Applying a first-order Taylor series expansion and neglecting higher-order terms yields the following linear discrete-time representations:

$$\mathbf{X}_{k+1} = \mathbf{\Phi}_k \mathbf{X}_k + \mathbf{w}_k \tag{51}$$

$$\mathbf{Z}_k = \mathbf{H}_k \mathbf{X}_k + \mathbf{v}_k \tag{52}$$

where $\mathbf{\Phi}_k$ and $\mathbf{H}_k$ denote the discrete-time state-transition and measurement matrices, respectively, given by the corresponding Jacobians as follows.

$$\mathbf{\Phi}_k = \left. \frac{\partial f(\mathbf{X}_k)}{\partial \mathbf{X}_k} \right|_{\mathbf{X}_k = \hat{\mathbf{X}}_k} \tag{53}$$

$$\mathbf{H}_k = \left. \frac{\partial h(\mathbf{X}_k)}{\partial \mathbf{X}_k} \right|_{\mathbf{X}_k = \hat{\mathbf{X}}_k^-} \tag{54}$$

Accordingly, the EKF equations can be expressed as follows [43,44]:

$$\hat{\mathbf{X}}_k^- = \mathbf{\Phi}_{k-1}\hat{\mathbf{X}}_{k-1} \tag{55}$$

$$\mathbf{P}_k^- = \mathbf{\Phi}_{k-1}\mathbf{P}_{k-1}\mathbf{\Phi}_{k-1}^T + \mathbf{Q}_w \tag{56}$$

$$\mathbf{s}_k = \mathbf{H}_k\mathbf{P}_k^-\mathbf{H}_k^T + \mathbf{R}_w \tag{57}$$

$$\mathbf{K}_a = \mathbf{P}_k^-\mathbf{H}_k^T\mathbf{s}_k^{-1} \tag{58}$$

$$\mathbf{P}_k = (\mathbf{I} - \mathbf{K}_k\mathbf{H}_k)\mathbf{P}_k^- \tag{59}$$

$$\hat{\mathbf{Z}}_k = \mathbf{Z}_k - \mathbf{H}\hat{\mathbf{X}}_k^- \tag{60}$$

$$\hat{\mathbf{X}}_k = \hat{\mathbf{X}}_k^- + \mathbf{K}_a\hat{\mathbf{Z}}_k \tag{61}$$

where $\mathbf{K}_a$ is the Kalman gain, $\mathbf{P}_k$ is the updated error covariance matrix, $\mathbf{s}_k$ is the innovation (residual) covariance matrix, and $\hat{\mathbf{Z}}_k$ denotes the innovation (measurement residual) sequence. The measurement-noise covariance matrix is given by $\mathbf{R}_w = \mathbf{I} \times R_w$, and the process-noise covariance matrix is given by $\mathbf{Q}_w = \mathbf{I} \times Q_w$. Repeating the computations in Equations (55)–(61) yields the recursive implementation of the EKF.

4.2. Input Estimation Combines EKF Method

For ballistic missile state estimation in the presence of lateral acceleration, a conventional EKF formulation without input terms is inadequate when the acceleration is not directly measured or known. To overcome this limitation, a recursive input estimation approach is employed to estimate the unknown lateral acceleration. The estimated input is subsequently incorporated into an EKF with input terms, thereby enhancing the accuracy of the state estimation. The proposed recursive input estimation scheme combines an EKF with a least-squares estimator (EKF + IE). The associated computational procedure is summarized in the following steps.

Consider a continuous-time system with input terms, whose state and measurement equations are expressed as Equations (62) and (63).

$$\dot{\mathbf{X}}(t) = \mathbf{A}\mathbf{X}(t) + \mathbf{B}\mathbf{u}(t) \tag{62}$$

$$\mathbf{Z}(t) = \mathbf{H}\mathbf{X}(t) + \mathbf{v}(t) \tag{63}$$

Considering the EKF formulation without input terms given in Equations (55)–(61), the measurement vector $\mathbf{Z}_k$ represents the output of the true system states and therefore implicitly contains stochastic variations induced by unknown time-varying inputs as well as measurement noise. The quantity $\hat{\mathbf{X}}_k$ denotes the state estimate obtained from the EKF without input terms. Accordingly, as shown in Equation (60), the innovation (residual) sequence $\hat{\mathbf{Z}}_k$ also contains stochastic information associated with the unknown time-varying inputs and measurement errors. Exploiting this property, the unknown time-varying inputs can be estimated using an online least-squares approach. The resulting recursive least-squares (RLS) algorithm is summarized as follows [45].

$$\mathbf{B}_k = \mathbf{H}(\mathbf{\Phi}_{k-1}\mathbf{M}_{k-1} + \mathbf{I})\mathbf{\Gamma} \tag{64}$$

$$\mathbf{M}_k = (\mathbf{I} - \mathbf{K}_a\mathbf{H})(\mathbf{\Phi}_{k-1}\mathbf{M}_{k-1} + \mathbf{I}) \tag{65}$$

$$\mathbf{K}_b = \gamma^{-1}\mathbf{P}_{k-1}^-\mathbf{B}_k^T\left[\mathbf{B}_k\gamma^{-1}\mathbf{P}_{k-1}^-\mathbf{B}_k^T + \mathbf{s}_k\right]^{-1} \tag{66}$$

$$\mathbf{P}_k^- = (\mathbf{I} - \mathbf{K}_b\mathbf{B}_k)\gamma^{-1}\mathbf{P}_{k-1}^- \tag{67}$$

$$\hat{\mathbf{u}}_k = \hat{\mathbf{u}}_{k-1} + \mathbf{K}_b\left[\hat{\mathbf{Z}}_k - \mathbf{B}_k\hat{\mathbf{u}}_{k-1}\right] \tag{68}$$

In the preceding formulation, $\hat{\mathbf{u}}_k$ denotes the estimated input, and $\mathbf{P}_k^-$ represents the covariance of the input estimation error. The matrix $\mathbf{K}_b$ is the input correction gain, whereas $\mathbf{B}_k$ and $\mathbf{M}_k$ denote the corresponding input and measurement sensitivity matrices. The matrix $\mathbf{K}_a$ represents the Kalman gain, and γ is a weighting factor. Because the system input $\hat{\mathbf{u}}_k$ is obtained from the least-squares estimator, it can be incorporated into the Kalman filter formulation with input terms to perform state correction, as shown in Equations (69) and (70). Consequently, improved state estimation accuracy is achieved.

$$\hat{\mathbf{X}}_k^- = \mathbf{\Phi}_{k-1}\hat{\mathbf{X}}_{k-1} + \mathbf{\Gamma}\hat{\mathbf{u}}_{k-1} \tag{69}$$

$$\hat{\mathbf{X}}_k = \hat{\mathbf{X}}_k^- + \mathbf{K}_a\hat{\mathbf{Z}}_k \tag{70}$$

The estimation of unknown inputs using the proposed input estimation approach can be summarized in the following four steps [44]:

(1) The continuous-time state and measurement equations given in Equations (62) and (63) are discretized, and the discrete-time measurement vector $\mathbf{z}_k$ is obtained.
(2) The updated error covariance matrix $\mathbf{S}_k$, the Kalman gain $\mathbf{K}_a$, and the innovation sequence $\hat{\mathbf{Z}}_k$ are computed using the Kalman filter Equations (55)–(61).
(3) The unknown system input $\hat{\mathbf{u}}_k$ is estimated using the recursive least-squares algorithm defined in Equations (64)–(68).
(4) The estimated input $\hat{\mathbf{u}}_k$ is substituted into Equations (69) and (70) to perform the state estimate correction.

The computational flow of the proposed EKF + IE method integrated with the IP-SOG scheme for target interception is illustrated in Figure 5. Following the estimation of the system input, namely the ballistic missile lateral acceleration, the estimated input is incorporated into the EKF with explicit input terms to refine the state estimates. As a result, more accurate positional information of the ballistic missile is obtained. The refined state estimates are subsequently provided to the IPSOG algorithm for guidance command generation, enabling effective target interception.

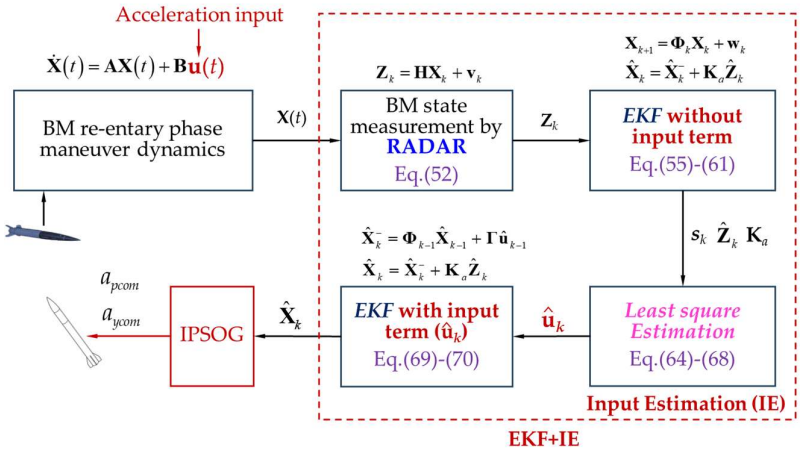


Figure 5. Computational flow of the integrated EKF + IE method and IPSOG scheme.

5. Simulation Results and Analysis

5.1. Ballistic Missile Trajectory Simulation

Two ballistic missile flight scenarios, namely, maneuvering and non-maneuvering trajectories, are considered in this study. The maneuvering trajectory is generated using an optimal guidance strategy that enforces accurate target interception, a terminal flight-path angle of −90 deg, and a maximum angle-of-attack constraint of 25 deg, while minimizing velocity loss as the performance index. In contrast, the non-maneuvering trajectory assumes zero lateral acceleration, with only gravitational and aerodynamic drag effects taken into account. The initial conditions for both scenarios are listed in Tables 1 and 2, and the corresponding flight trajectories are depicted in Figures 6 and 7.

Table 1. Initial conditions for the maneuvering ballistic missile.

Parameter (Unit)	Value	Parameter (Unit)	Value
X Position (m)	10,000	Mass (kg)	600
Y Position (m)	−70,000	Reference Area (m^2)	0.754
Z Position (m)	45,000	Earth Radius (m^2)	6,378,140
Longitudinal Velocity (m/s)	3870	Zero-Lift Drag Coefficient C_{x0}	0.0774
Pitch Angle (deg)	−45	Drag Derivative C_x^α (1/deg)	0.00084
Yaw Angle (deg)	0	Lift Derivative C_y^α (1/deg)	0.0333

Table 2. Initial conditions for the non-maneuvering ballistic missile.

Parameter (Unit)	Value	Parameter (Unit)	Value
X Position (m)	10,000	Yaw Angle (deg)	0
Y Position (m)	−70,000	Mass (kg)	600
Z Position (m)	45,000	Reference Area (m^2)	0.754
Longitudinal Velocity (m/s)	3870	Zero-Lift Drag Coefficient C_{x0}	0.0774
Pitch Angle (deg)	−45	Gravitational Acceleration (m/s^2)	9.8

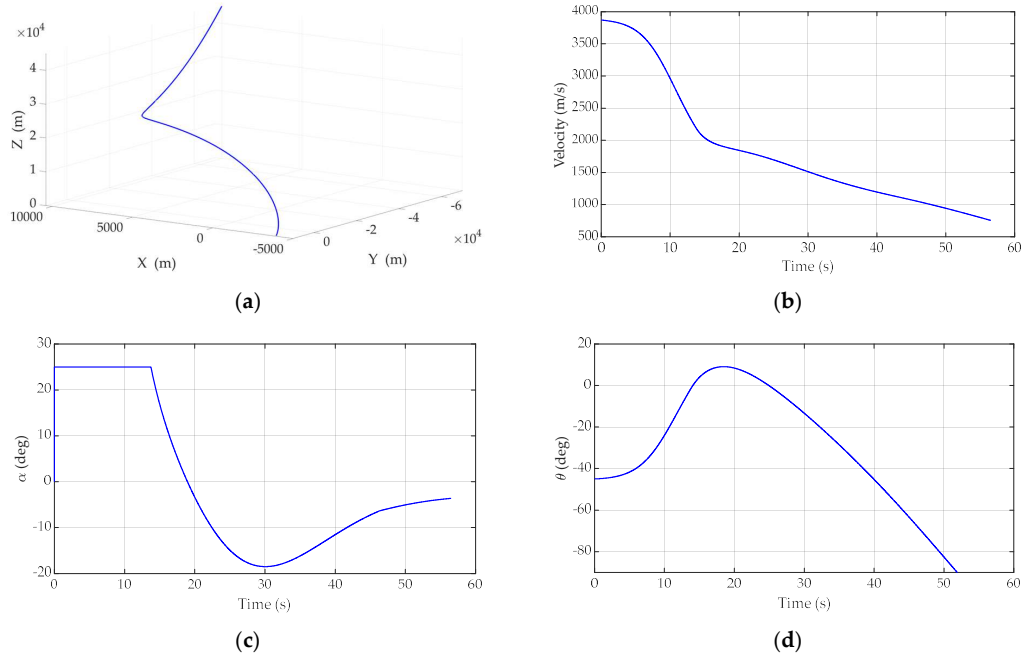


Figure 6. Maneuvering ballistic missile trajectory and state histories versus time: (**a**) three-dimensional trajectory, (**b**) velocity, (**c**) angle of attack, and (**d**) flight-path angle.

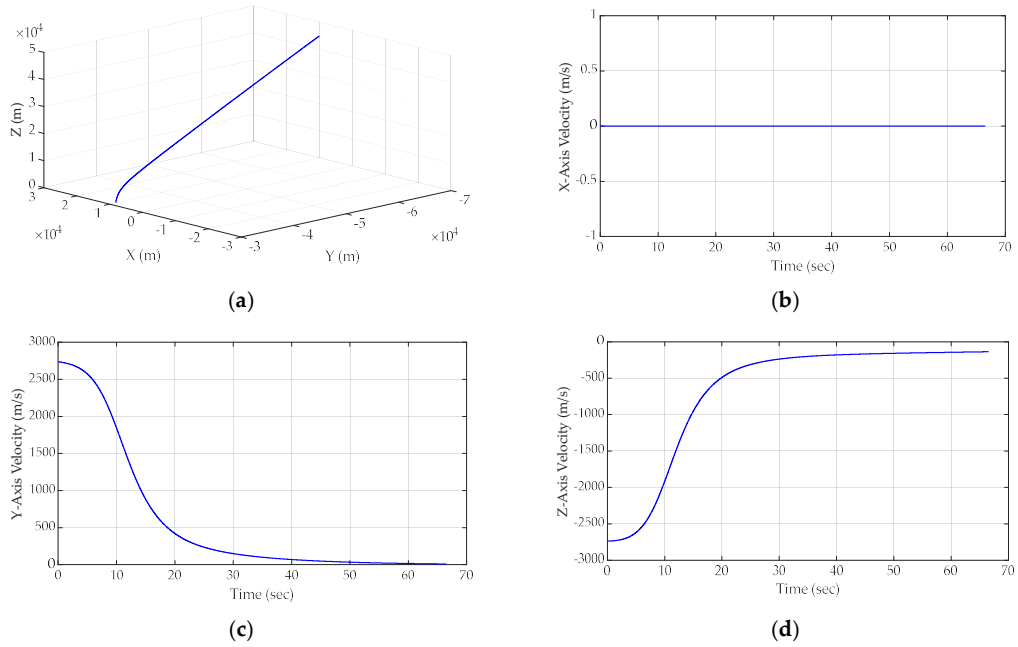


Figure 7. Non-maneuvering ballistic missile trajectory and velocity histories versus time: (**a**) three-dimensional trajectory, (**b**) *X*-axis, (**c**) *Y*-axis, and (**d**) *Z*-axis.

Figure 6a shows the maneuvering trajectory under the constraints of reaching the prescribed target location with a −90 deg flight-path angle at impact. The maneuver includes both longitudinal and lateral deviations. Figure 6b–d present the time histories of BM velocity, angle of attack, and flight-path angle during the maneuver. A rapid change in angle of attack occurs at approximately 13 s, indicating the onset of significant lateral acceleration.

Figure 7a presents the trajectory of the non-maneuvering warhead under the same terminal constraint of a −90 deg flight-path angle at impact. Figure 7b–d show the time histories of the velocity components along each coordinate axis. A pronounced deceleration is observed prior to approximately 30 s, indicating the onset of significant aerodynamic drag. Figures 6a and 7a further confirm that both maneuvering and non-maneuvering trajectories satisfy the terminal flight-path angle constraint of −90 deg.

Figure 8 compares maneuvering and non-maneuvering BM trajectories attacking the same fixed ground target, demonstrating that markedly different flight paths can achieve the same impact point. From the attacker's perspective, either trajectory type may be employed with different initial reentry conditions, providing flexibility in selecting a safer reentry location that avoids ballistic missile defense regions and enhances penetration capability.

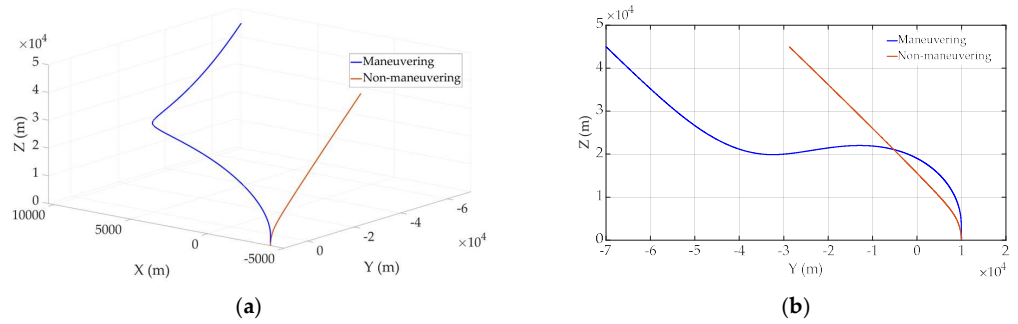


Figure 8. Comparison of maneuvering and non-maneuvering warhead trajectories attacking the same fixed ground target: (**a**) three-dimensional trajectory and (**b**) projection onto the *Y*–*Z* plane.

Figure 9 presents the case in which both missiles attack the target from the same initial reentry condition. From the defender's perspective, the impact point of a non-maneuvering missile can be more readily inferred from ground-based radar measurements. In contrast, a maneuvering missile deviates from its nominal trajectory through optimal guidance, rendering its future flight path less predictable and increasing the difficulty of interception.

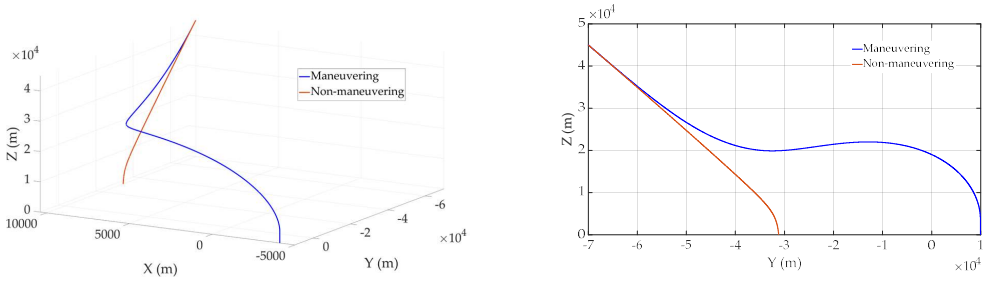


Figure 9. Comparison of maneuvering and non-maneuvering warhead trajectories with the same initial reentry conditions: (**a**) three-dimensional trajectory and (**b**) projection onto the *Y*–*Z* plane.

5.2. Ballistic Missile Trajectory Estimation

5.2.1. Maneuvering Trajectory Estimation

The ballistic missile trajectory is propagated using a Runge–Kutta integration scheme, with additive Gaussian white noise introduced to simulate realistic radar measurement uncertainty. An EKF and an EKF + IE method are employed for state estimation, and their performances are compared. The EKF parameters are set as follows: measurement noise covariance $R_w = 5$, time step $\Delta t = 0.01$ s, and forgetting factor $\gamma = 0.85$. The forgetting factor may introduce different levels of delay in the input estimation results, as discussed in Ref. [24].

Figures 10–12 present the position estimation errors for different values of the system noise covariance Q_w. The results indicate that a smaller covariance ($Q_w = 10$) yields larger estimation errors with reduced fluctuation, whereas a larger covariance ($Q_w = 10^{2.5}$) decreases the error magnitude at the cost of increased oscillations. To achieve a balance between estimation accuracy and stability, $Q_w = 10^{1.5}$ is adopted.

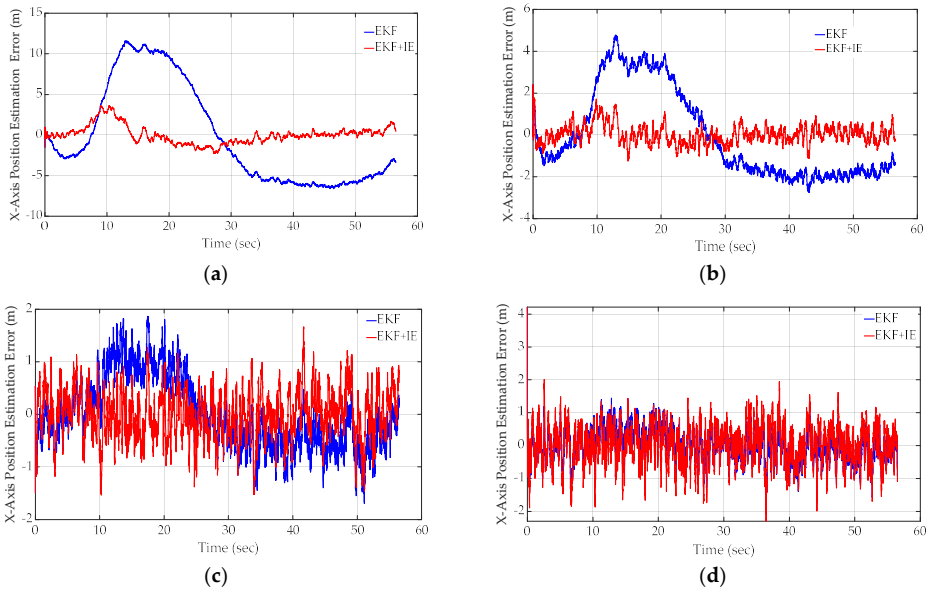


Figure 10. *X*-axis position estimation error under different system noise covariance values Q_w: (**a**) $Q_w = 10$; (**b**) $Q_w = 10^{1.5}$; (**c**) $Q_w = 10^2$; (**d**) $Q_w = 10^{2.5}$.

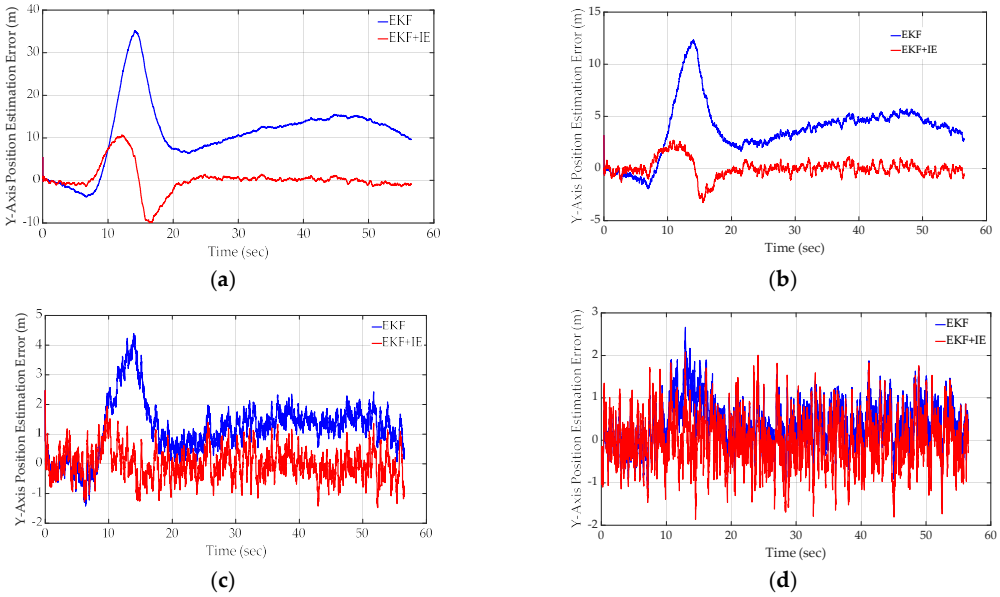


Figure 11. Y-axis position estimation error under different system noise covariance values Q_W: (**a**) $Q_w = 10$; (**b**) $Q_w = 10^{1.5}$; (**c**) $Q_w = 10^2$; (**d**) $Q_w = 10^{2.5}$.

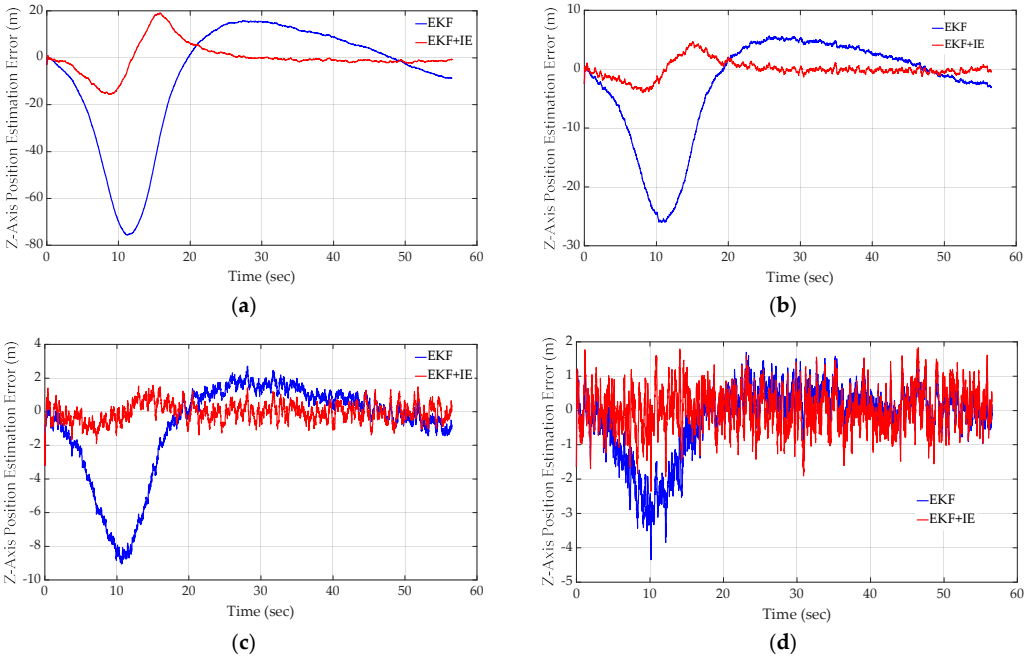


Figure 12. Z-axis position estimation error under different system noise covariance values Q_w: (**a**) $Q_w = 10$; (**b**) $Q_w = 10^{1.5}$; (**c**) $Q_w = 10^2$; (**d**) $Q_w = 10^{2.5}$.

With $Q_w = 10^{1.5}$, the EKF position estimation errors range approximately from -2 to 4 m along the X-axis, -2 to 12 m along the Y-axis, and -25 to 5 m along the Z-axis. In contrast, the EKF + IE estimates remain within approximately ± 1 m, ± 3 m, and ± 5 m along the X-, Y-, and Z-axes, respectively. Overall, the EKF + IE approach significantly outperforms the EKF in all axes. The inferior performance of the EKF is attributed to unmodeled lateral acceleration during missile flight, as the EKF formulation neglects input terms. As a result, larger estimation errors arise, particularly during periods of high lateral acceleration (0–30 s), which would adversely affect interceptor guidance performance. To mitigate this deficiency, the IE method is used to estimate the lateral acceleration, which is then incorporated into a EKF with input modeling. This approach substantially reduces the estimation errors. As shown in Figure 13, the estimated lateral acceleration closely

matches the true acceleration, demonstrating the effectiveness of the proposed method and its potential to enhance interception success probability.

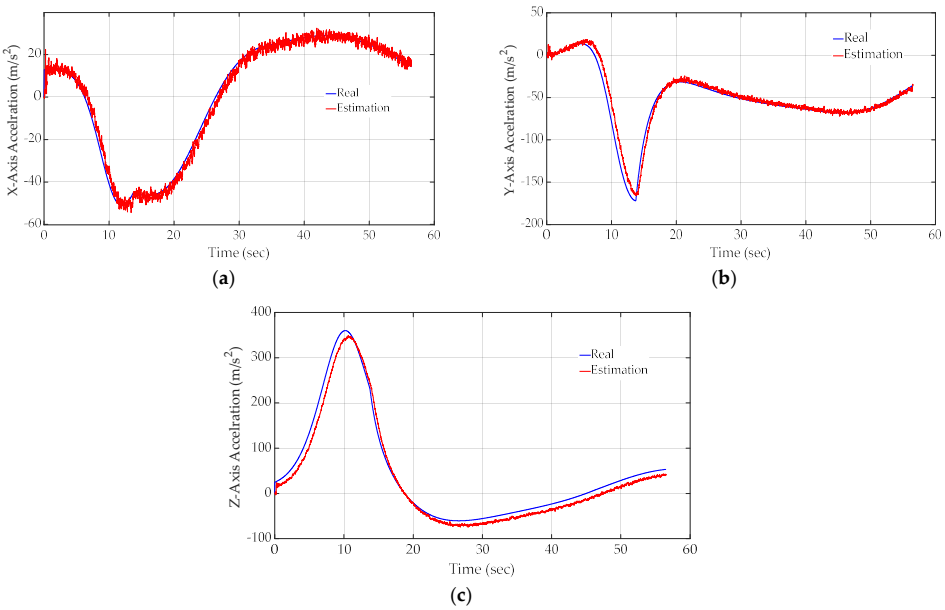


Figure 13. Acceleration estimation results along the three axes for the maneuvering trajectory using the IE method: (**a**) *X*-axis, (**b**) *Y*-axis, and (**c**) *Z*-axis.

5.2.2. Non-Maneuvering Trajectory Estimation

Using the parameter settings listed in Table 2, Figure 14 shows the state estimation errors for a non-maneuvering missile trajectory obtained using the EKF and EKF + IE methods. The estimation errors along the *X*-axis are relatively small, as both the velocity and lateral acceleration in this direction are zero. In contrast, the *Y*- and *Z*-axis errors are more pronounced due to lateral accelerations induced by aerodynamic drag, particularly during the interval from 0 to 30 s. Figure 14 further indicates that the EKF + IE method yields smaller overall estimation errors than the EKF, demonstrating its superior accuracy in estimating the true states.

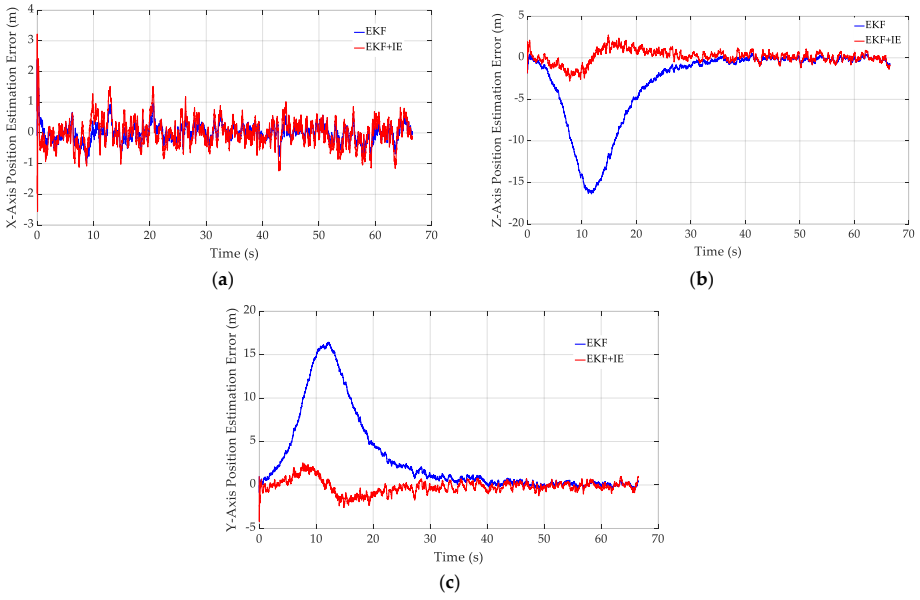


Figure 14. Position estimates along the three axes for a non-maneuvering missile trajectory using the EKF and EKF + IE methods: (**a**) *X*-axis, (**b**) *Y*-axis, and (**c**) *Z*-axis.

5.3. Interception Performance Analysis

This section examines the interception of maneuvering and non-maneuvering ballistic missiles under noisy conditions using PNG and an IPSOG integrated with EKF and EKF + IE architectures. Four simulation scenarios are conducted to evaluate interception performance in terms of miss distance, time-to-go (T_{go}), and average lateral acceleration in pitch and yaw.

A successful interception is defined as a miss distance less than the lethal radius of the interceptor warhead, set to 20 m. The initial missile positions for the four scenarios are listed in Table 3. The missile is modeled as a point mass; thus, aerodynamic and other physical parameters are not required. The interceptor initial parameters are summarized in Table 4, and the particle swarm optimization settings are given in Table 5. To mitigate premature convergence to a local optimum, the initial particle positions are distributed across the four quadrants of the two-dimensional lateral acceleration solution space before the search process. Under this configuration, the optimal solution typically converges within 0.02 s while reducing the likelihood of local entrapment. The resulting interception performance metrics are reported in Tables 6–9, and the corresponding interception trajectories are shown in Figures 15–18.

Table 3. BM Initial Positions for Four Simulation Scenarios.

Parameter (Unit)	Maneuvering Scenario		Non-Maneuvering Scenario	
	Scenario 1	**Scenario 2**	**Scenario 3**	**Scenario 4**
X Position (m)	11,000	6000	19,000	22,000
Y Position (m)	−68,000	−64,000	10,000	12,000
Z Position (m)	47,000	48,000	20,000	40,000

Table 4. Initial States and Parameters of the ABM.

Parameter (Unit)	Value	Parameter (Unit)	Value
X Position (m)	0	Lateral acceleration limit (g)	±30
Y Position (m)	0	Navigation constant	3
Z Position (m)	0	Time step (s)	0.01
Yaw angle (deg)	0	Time constant (s)	0.1
Pitch angle (deg)	90	Lethal radius (m)	20
Longitudinal velocity (m/s)	1463	Gravitational acceleration (m/s^2)	9.8

Table 5. Initial parameters of the particle swarm optimization algorithm.

Parameter		Value	Parameter		Value
Maximum number of iterations		500	Standard deviation		10^{-2}
Total number of particles		100	Learning factor c_1	Initial value	2.5
				Final value	0.5
Inertia weight	Upper bound	1.5	Learning factor c_2	Initial value	0.5
	Lower bound	0.5		Final value	2.5

Table 6. Interception performance comparison for maneuvering ballistic missiles using different guidance laws and filtering approaches in Scenario 1.

Filter	Guidance Law	Miss Distance (m)	Intercept Time (s)	Average Lateral Acceleration (g)		Interception Result
				Pitch	Yaw	
EKF	PNG	17.14	23.1	29.94	22.26	Success
	IPSOG	13.73	20.3	27.89	19.94	Success
EKF + IE	PNG	15.73	22.86	29.93	22.89	Success
	IPSOG	10.21	21.57	26.86	19.59	Success

Table 7. Interception performance comparison for maneuvering ballistic missiles using different guidance laws and filtering approaches in Scenario 2.

Filter	Guidance Law	Miss Distance (m)	Intercept Time (s)	Average Lateral Acceleration (g)		Interception Result
				Pitch	Yaw	
EKF	PNG	2223.00	19.40	30.00	24.33	Failure
	IPSOG	15.46	19.03	27.07	20.15	Success
EKF + IE	PNG	124.94	20.36	29.99	23.89	Failure
	IPSOG	10.86	18.87	26.75	19.72	Success

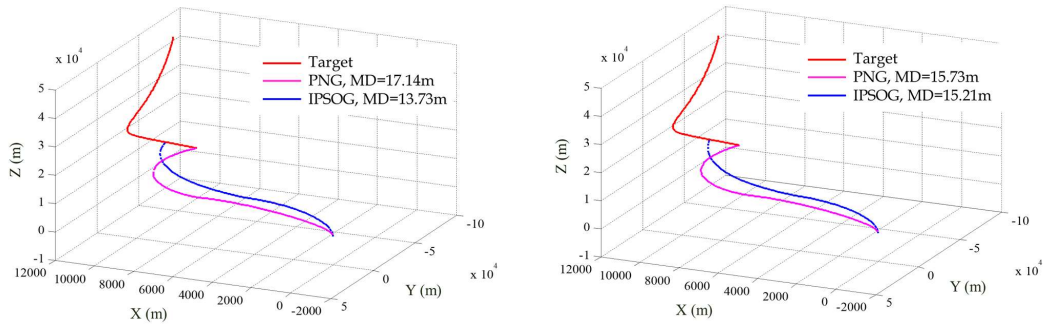
Table 8. Interception performance comparison for non-maneuvering ballistic missiles using different guidance laws and filtering approaches in Scenario 3.

Filter	Guidance Law	Miss Distance (m)	Intercept Time (s)	Average Lateral Acceleration (g)		Interception Result
				Pitch	Yaw	
EKF	PNG	18.20	10.81	29.94	30.00	Success
	IPSOG	8.59	11.30	28.00	19.75	Success
EKF + IE	PNG	17.37	10.79	29.96	29.96	Success
	IPSOG	5.82	11.32	27.95	19.74	Success

Table 9. Interception performance comparison for non-maneuvering ballistic missiles using different guidance laws and filtering approaches in Scenario 4.

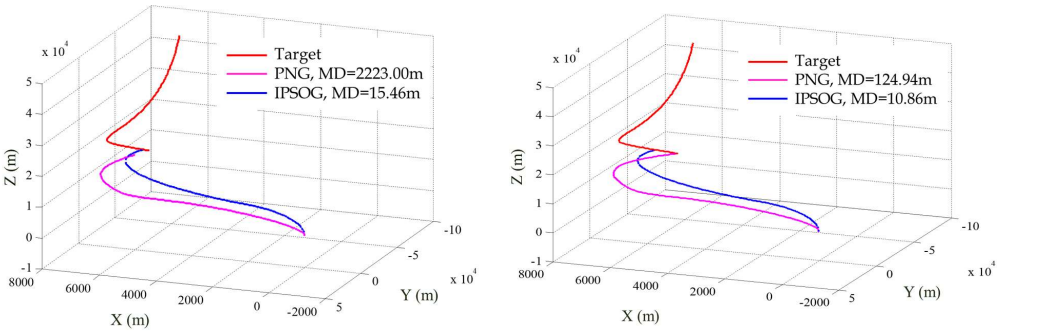
Filter	Guidance Law	Miss Distance (m)	Intercept Time (s)	Average Lateral Acceleration (g)		Interception Result
				Pitch	Yaw	
EKF	PNG	1508.60	14.89	28.71	29.98	Failure
	IPSOG	11.57	13.50	28.56	22.68	Success
EKF + IE	PNG	790.45	14.14	28.63	29.02	Failure
	IPSOG	10.61	13.36	27.95	21.65	Success

As summarized in Table 6, both PNG and IPSOG successfully intercept the target in Scenario 1. When either EKF or EKF + IE is employed, IPSOG achieves a smaller miss distance, demonstrating improved terminal interception accuracy. In addition, IPSOG yields a shorter time-to-intercept, which contributes to reduced propellant consumption during the engagement. As shown in Figures 15 and 16, when the BM performs a large maneuver and deviates significantly from its nominal trajectory, PNG commands a substantially larger turning angle than IPSOG, resulting in a longer interceptor flight path. Overall, these results demonstrate that IPSOG provides superior guidance performance compared with PNG.



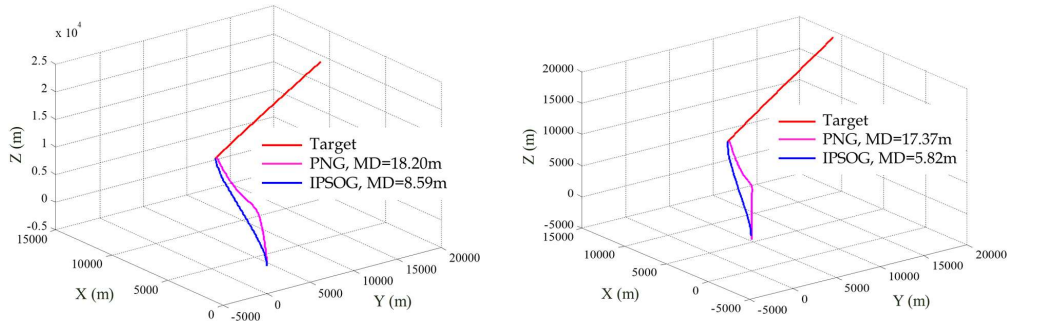
(**a**) (**b**)

Figure 15. Interception trajectories of maneuvering ballistic missiles under PNG and IPSOG with different filters in Scenario 1: (**a**) EKF and (**b**) EKF + IE.



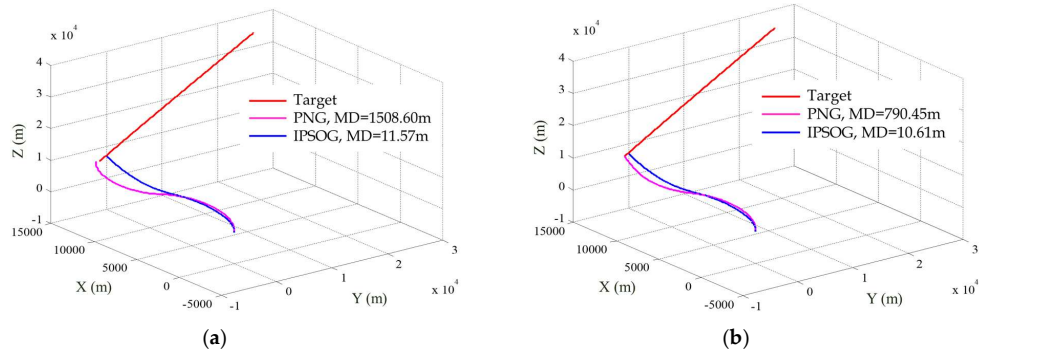
(**a**) (**b**)

Figure 16. Interception trajectories of maneuvering ballistic missiles under PNG and IPSOG with different filters in Scenario 2: (**a**) EKF and (**b**) EKF + IE.



(**a**) (**b**)

Figure 17. Interception trajectories of non-maneuvering ballistic missiles under PNG and IPSOG with different filters in Scenario 3: (**a**) EKF and (**b**) EKF + IE.



(**a**) (**b**)

Figure 18. Interception trajectories of non-maneuvering ballistic missiles under PNG and IPSOG with different filters in Scenario 4: (**a**) EKF and (**b**) EKF + IE.

In Scenario 2, PNG fails to intercept the target, whereas IPSOG maintains successful interception, indicating a wider effective interception region for IPSOG. A comparison of the interception processes in Scenarios 1 and 2 shows that PNG fails to intercept the target in Scenario 2. This behavior is primarily influenced by the relative distance between the missile and the target when the target initiates the maneuver. When the separation distance is large (Scenario 1), the missile has sufficient time to adjust its trajectory and achieve interception. In contrast, when the distance is short (Scenario 2), the missile must rapidly change its flight direction within a limited distance, which may lead to a larger miss distance and interception failure. These results indicate that PNG with a fixed guidance constant has limited capability for intercepting targets undergoing sudden maneuvers.

As indicated in Table 8, in Scenario 3, where both guidance laws successfully intercept the target, IPSOG achieves a smaller miss distance and a lower average lateral acceleration when EKF + IE and EKF are employed. Figures 17 and 18, together with the data summarized in Table 9, further shows that PNG fails to intercept the target in Scenario 4. This behavior is mainly attributed to the larger lateral separation during the engagement, which produces a more pronounced side-interception geometry under PNG. When the missile speed is lower than that of the target, this geometry can lead to a larger miss distance and interception failure. These results indicate that PNG with a fixed guidance constant has limited capability for intercepting targets with large lateral separation.

6. Conclusions and Future Work

6.1. Conclusions

This study investigated an integrated state estimation and guidance framework for missile defense applications against both maneuvering and non-maneuvering ballistic missiles. An EKF combined with an IE technique (EKF + IE) was employed to construct a ballistic missile trajectory estimator, and the simulation results demonstrate improved state observability and estimation accuracy, enabling more accurate reconstruction of target motion states for reliable interceptor guidance. An IPSOG was applied to the interceptor missile and evaluated against conventional PNG in both maneuvering and non-maneuvering engagement scenarios. The results indicate that IPSOG achieves reduced miss distance, shorter time-to-intercept, lower average lateral acceleration, and a significantly expanded interception region. The reduced lateral acceleration demand also contributes to lower structural loads on the interceptor, thereby enhancing system robustness and survivability. Overall, the integrated architecture combining EKF + IE state estimation with IPSOG increases interception success probability and system efficiency, providing a practical and scalable design reference for missile defense systems tasked with countering maneuvering ballistic missile threats.

6.2. Future Work

This study integrates a state observer, an input estimator, and a guidance law to develop a guidance framework capable of intercepting high-speed maneuvering ballistic missiles with trajectory variations. Several research directions may be pursued to further extend the present work.

First, the interceptor missile is modeled as a point-mass system, and several practical factors relevant to missile defense applications are not considered, including mass variation due to fuel consumption, time-varying thrust, and altitude-dependent aerodynamic drag. Incorporating these effects into the interceptor equations of motion would enable a more realistic representation of engagement conditions and allow further evaluation of interception performance under operational constraints. In addition, lateral acceleration commands are generated using particle swarm optimization (PSO) at each guidance update. Although

the IPSOG law demonstrates improved interception performance, PSO-based methods may exhibit premature convergence during the early search stage, which can lead to large transient acceleration commands. Such behavior may violate actuator limits or adversely affect structural integrity. Future work will therefore investigate hybrid guidance strategies in which proportional navigation or other robust guidance laws are employed during the initial engagement phase, followed by IPSOG in the terminal phase.

Furthermore, the input estimation (IE) technique is incorporated into the filtering framework to mitigate estimation errors caused by unknown system inputs and to improve state estimation accuracy. Consequently, comparisons among different filtering algorithms are beyond the scope of this study. Future studies may integrate the IE technique with other filtering approaches, such as the Unscented Kalman Filter (UKF) or Particle Filter (PF), to evaluate its applicability across different filtering frameworks. In addition, the effects of non-Gaussian measurement noise and low-observability conditions are not considered in this work. Investigating these issues may further improve estimation performance and enhance the applicability of passive sensing systems in highly maneuvering target interception scenarios.

Author Contributions: Conceptualization, Y.-L.L. and W.-Y.Y.; methodology, Y.-L.L.; software, W.-Y.Y.; validation, Y.-L.L.; formal analysis, Y.-L.L.; investigation, W.-Y.Y.; resources, Y.-L.L.; data curation, W.-Y.Y.; writing—original draft preparation, Y.-L.L.; writing—review and editing, Y.-L.L.; visualization, Y.-L.L. and W.-Y.Y.; supervision, Y.-L.L.; project administration, Y.-L.L.; funding acquisition, W.-Y.Y. and Y.-L.L. All authors have read and agreed to the published version of the manuscript.

Funding: This research received no external funding.

Institutional Review Board Statement: Not applicable.

Informed Consent Statement: Not applicable.

Data Availability Statement: The original contributions presented in the study are included in the article, further inquiries can be directed to the corresponding author.

Conflicts of Interest: The authors declare no conflicts of interest.

Abbreviations

ABM	Anti-Ballistic Missile
AKF	Adaptive Kalman Filter
BM	Ballistic Missile
CADFT	Covariance Analysis Describing Function Technique
CLOS	Command-to-Line-of-Sight
CRLB	Cramér–Rao Lower Bound
EKF	Extended Kalman Filter
FWIEM	Fuzzy Weighting Input Estimation Method
GLSM	Generalized Least Squares Method
IE	Input Estimation
IPSOG	Improved Particle Swarm Optimization Guidance Law
LOS	Line-of-Sight
PNG	Proportional Navigation Guidance Law
PSO	Particle Swarm Optimization
PSOG	Particle Swarm Optimization Guidance Law
RAC	Radar Area Correlation
RLSE	Recursive Least Squares Estimator
RV	Reentry Vehicle
STT	Skid-To-Turn
UKF	Unscented Kalman Filter

References

1. Lund, F.H. Evolution of the Pershing II Missile System. In Proceedings of the Guidance and Control Conference, Technical Papers (A84-43401 21-63), Seattle, WA, USA, 20–22 August 1984; pp. 693–703.
2. Erickson, A.S.; Yang, D.D. Using the Land to Control the Sea?—Chinese Analysts Consider the Antiship Ballistic Missile. *Nav. War Coll. Rev.* **2009**, *62*, 53–86.
3. Liu, K.F.; Meng, H.D.; Wang, C.J.; Li, J.; Chen, Y. Anti-Head-on Interception Penetration Guidance Law for Slide Vehicle. *Mod. Def. Technol.* **2008**, *4*, 39–45.
4. Jiang, L.; Nan, Y.; Zhang, Y.; Li, Z. Anti-Interception Guidance for Hypersonic Glide Vehicle: A Deep Reinforcement Learning Approach. *Aerospace* **2022**, *9*, 424. [CrossRef]
5. Cunyu, B.; Peng, W.; Guojian, T. Integrated Method of Guidance, Control and Morphing for Hypersonic Morphing Vehicle in Glide Phase. *Chin. J. Aeronaut.* **2021**, *34*, 535–553. [CrossRef]
6. Luo, X.; Li, J. Fuzzy Dynamic Characteristic Model-based Attitude Control of Hypersonic Vehicle in Gliding Phase. *Sci. China Inf. Sci.* **2011**, *54*, 448–459. [CrossRef]
7. Tian, Z.; Yang, K.; Danino, M.; Bar-Shalom, Y.; Milgrom, B. Ballistic Object Trajectory and Impact Point Estimation in the Reentry Phase From a Moving Passive Sensor. *IEEE Trans. Aerosp. Electron. Syst.* **2022**, *58*, 4540–4550. [CrossRef]
8. Tian, Z.; Yang, K.; Danino, M.; Bar-Shalom, Y.; Milgrom, B. Missile motion Parameter Estimation with a Passive Sensor from a High Speed Aircraft. In Proceedings of the Signal Processing, Sensor/Information Fusion, and Target Recognition XXXI, Orlando, FL, USA, 3–7 April 2022.
9. Tian, Z.; Yang, K.; Danino, M.; Bar-Shalom, Y.; Milgrom, B. Pursuer Aim Identification for an Aircraft Formation Using a Passive Sensor Without State Estimation. *IEEE Trans. Aerosp. Electron. Syst.* **2022**, *58*, 1176–1186. [CrossRef]
10. Hu, Z.D.; Cao, Y.; Cai, H. Variable Structure Guidance Law of Reentry Maneuvering Warhead with Terminal Angular Constraint. *Syst. Eng. Electron.* **2009**, *31*, 393–398.
11. Tziallas, G.; Adam, M.; Assimakis, N. Position, Velocity and Acceleration Tracking Using Kalman Filter. *Theory Pract. Math. Comput. Sci.* **2021**, *9*, 30–47.
12. Yu, T.Y.; Wu, C.M. Application of Adaptive α-β-γ and α-β-γ-δ Filters to Tracking Systems. *Sens. Mater.* **2017**, *29*, 419–427.
13. Khan, J.; Kim, K. A Performance Evaluation of the Alpha-Beta (α-β) Filter Algorithm with Different Learning Models: DBN, DELM, and SVM. *Appl. Sci.* **2022**, *12*, 9429. [CrossRef]
14. Greg, W.; Gary, B. *An Introduction to the Kalman Filter*; University of North Carolina at Chapel Hill: Chapel Hill, NC, USA, 2001.
15. Li, J.; Xu, X.; Jiang, Z.; Jiang, B. Adaptive Kalman Filter for Real-Time Visual Object Tracking Based on Autocovariance Least Square Estimation. *Appl. Sci.* **2024**, *14*, 1045. [CrossRef]
16. Shi, J.G.; Xu, M.Y.; Wang, Z.Y.; Zhang, B.L. Application of Kalman Filtering in Calculation of Trajectory Falling Point of Trajectory Correction Projectiles. *J. Ballist.* **2008**, *20*, 41–43.
17. Farina, A.; Ristic, B.; Benvenuti, D. Tracking a Ballistic Target: Comparison of Several Nonlinear Filters. *IEEE Trans. Aerosp. Electron. Syst.* **2002**, *38*, 854–867. [CrossRef]
18. Bar-Shalom, Y.; Chang, K.C.; Blom, H.A.P. Tracking a maneuvering target using input estimation versus the interacting multiple model algorithm. *IEEE Trans. Aerosp. Electron. Syst.* **1989**, *25*, 296–300. [CrossRef]
19. Chan, Y.T.; Hu, A.C.; Plant, J.B. A Kalman Filter Based Tracking Scheme with Input Estimation. *IEEE Trans. Aerosp. Electron. Syst.* **1979**, *AES-15*, 237–242. [CrossRef]
20. Bogler, T.L. Tracking a Maneuvering Target Using Input Estimation. *IEEE Trans. Aerosp. Electron. Syst.* **1987**, *AES-23*, 298–303. [CrossRef]
21. Mendel, J.M. *Lessons in Estimation Theory or Signal Processing, Communication, and Control*; Prentice-Hall PTR: Englewood Cliffs, NJ, USA, 1995.
22. Tuan, P.C.; Fong, L.W. An IMM Tracking Algorithm with Input Estimation. *Int. J. Syst. Sci.* **1996**, *27*, 629–639. [CrossRef]
23. Lee, S.C.; Liu, C.Y. Improved Trajectory Estimation of Reentry Vehicles from Radar Measurements Using On-line Adaptive Input Estimation. *IEICE Trans. Fundam.* **1998**, *E81-A*, 1867–1872.
24. Chen, T.C.; Lee, M.H. Intelligent Fuzzy Weighted Input Estimation Method Applied to Inverse Heat Conduction Problems. *Int. J. Heat Mass Transf.* **2008**, *58*, 4168–4183. [CrossRef]
25. Yang, C.D.; Yang, C.C. Optimal Pure Proportional Navigation for Maneuvering Targets. *IEEE Trans. Aerosp. Electron. Syst.* **1997**, *33*, 949–957. [CrossRef]
26. Kim, M.; Hong, D.; Park, S. Deep Neural Network-Based Guidance Law Using Supervised Learning. *Appl. Sci.* **2020**, *10*, 7865. [CrossRef]
27. Lee, S.C.; Soong, C.Y.; Tao, C.S.; Bu, J.T. A Generalized Guidance Method Design for Anti-Ballistic Missile in Collision Course. *Trans. Aeronaut. Astronaut. Soc. Repub. China* **1999**, *31*, 49–56. (In Chinese)

28. Tyan, F. Capture Region of a 3D PPN Guidance Law for Intercepting High-Speed Targets. *Asian J. Control* **2012**, *14*, 1215–1226. [CrossRef]
29. Shima, T.; Golan, O.M. Head Pursuit Guidance. *J. Guid. Control Dyn.* **2007**, *30*, 1437–1444. [CrossRef]
30. Prasanna, H.M.; Ghose, D. Retro-Proportional-Navigation: A New Guidance Law for Interception of High-Speed Targets. *J. Guid. Control Dyn.* **2012**, *35*, 377–386. [CrossRef]
31. Ghosh, S.; Ghose, D.; Raha, S. Capturability Analysis of a 3-D Retro-PN Guidance Law for Higher Speed Non-maneuvering Targets. *IEEE Trans. Control Syst. Technol.* **2014**, *22*, 1864–1874. [CrossRef]
32. Zhao, J.; Yan, L.; Li, Y. A Comparative Study of Head-Pursuit or Head-on Engagement Guidance Law Against High-Speed Target. *J. Equip. Acad.* **2014**, *26*, 68–73. (In Chinese)
33. Eberhart, R.; Kennedy, J. A New Optimizer Using Particle Swarm Theory. In Proceedings of the International Symposium on Micro Machine and Human Science, Nagoya, Japan, 4–6 October 1995; pp. 39–43.
34. Kennedy, J.; Eberhart, R. Particle Swarm Optimization. In Proceedings of the Fourth IEEE International Conference on Neural Networks, Perth, WA, Australia, 27 November–1 December 1995; pp. 1942–1948.
35. Eberhart, R.C.; Shi, Y. Particle Swarm Optimization: Developments, Applications and Resources. In Proceedings of the IEEE Congress on Evolutionary Computation, Seoul, Republic of Korea, 27–30 May 2001; pp. 81–86.
36. Shi, Y.; Eberhart, R.C. A Modified Particle Swarm Optimizer. In Proceedings of the IEEE Congress on Evolutionary Computation, Anchorage, AK, USA, 4–9 May 1998; pp. 69–73.
37. Kung, C.C.; Chen, K.Y. Missile Guidance Algorithm Design Using Particle Swarm Optimization. *Trans. Can. Soc. Mech. Eng.* **2013**, *37*, 971–979. [CrossRef]
38. Zarchan, P. *Tactical and Strategic Missile Guidance*, 7th ed.; American Institute of Aeronautics and Astronautics: Reston, VA, USA, 2019.
39. Chen, K.; Zhao, H. An Optimal Reentry Maneuver Guidance Law Applying to Attack the Ground Fixed Target. *J. Astronaut.* **1994**, *1*, 1–7. (In Chinese)
40. Chen, K.Y.; Lee, Y.L.; Liao, S.J.; Kung, C.C. The design of particle swarm optimization guidance using a line-of-sight evaluation method. *Comput. Electr. Eng.* **2016**, *54*, 159–169. [CrossRef]
41. Imado, F. Some Aspects of a Realistic Three-Dimensional Pursuit-Evasion Game. *J. Guid. Control Dyn.* **1993**, *16*, 289–293. [CrossRef]
42. Ratnaweera, A.; Halgamuge, S.K.; Watson, H.C. Self-Organizing Hierarchical Particle Swarm Optimizer with Time-Varying Acceleration Coefficients. *IEEE Trans. Evol. Computation* **2004**, *8*, 240–255. [CrossRef]
43. Yang, Z.; Shang, M.; Yin, J. Analytical Second-Order Extended Kalman Filter for Satellite Relative Orbit Estimation. *Aerospace* **2024**, *11*, 887. [CrossRef]
44. Herrera, L.; Méndez-Ramírez, R. Discrete Unilateral Constrained Extended Kalman Filter in an Embedded System. *Sensors* **2025**, *25*, 4636. [CrossRef]
45. Ma, C.K.; Chang, J.M.; Lin, D.C. Input Forces Estimation of Beam Structures by an Inverse Method. *J. Sound Vib.* **2003**, *259*, 387–407. [CrossRef]

Disclaimer/Publisher's Note: The statements, opinions and data contained in all publications are solely those of the individual author(s) and contributor(s) and not of MDPI and/or the editor(s). MDPI and/or the editor(s) disclaim responsibility for any injury to people or property resulting from any ideas, methods, instructions or products referred to in the content.